

AGN Jet-induced Feedback in Galaxies. I. Suppression of Star Formation.

V. Antonuccio-Delogu^{1,2*}, J. Silk¹

¹*Astrophysics, Department of Physics, University of Oxford, Keble Road Ox1 3RH, Oxford, United Kingdom*

²*INAF - Osservatorio Astrofisico di Catania, Via S. Sofia 78, Catania, I-95123, Italy*

Accepted ??, Received ??; in original form 2007 ??

ABSTRACT

Relativistic jets originating from Supermassive Black Holes (SBHs) can have a considerable impact on the Interstellar/Intergalactic Medium (ISM/IGM) within which they propagate. Here we study the interaction which a relativistic jet, and the cocoon associated with its penetration into the ISM, has on the evolution of a dense cloud, placed very near the cocoon's path, by analyzing a series of high-resolution numerical simulations, and studying the dependence on jet input power, between $P_{jet} = 10^{41} - 10^{47}$ erg/sec. The density Probability Distribution Function (PDF) within the cocoon can be described in terms of two distinct components, which are also spatially distinct: a low- and a high-density component. The former is associated with the shocked gas within the internal region of the cocoon, while the latter is associated with the outer, shocked region of the cocoon itself. The PDF of the post-shocked region is well approximated by a modified lognormal distribution, for all values of P_{jet} . During the *active* phase, when the jet is fed by the AGN, the cloud is subject both to compression and stripping, which tend to increase its density and diminish its total mass. When the jet is switched off (i.e. during the *passive* phase) the shocked cloud cools further and tends to become more filamentary, under the action of a back-flow which develops within the cocoon.

We study the evolution of the star formation rate within the cloud, assuming this is determined by a Schmidt-Kennicutt law, and we analyze the different physical factors which have an impact on the star formation rate. We show that, although the star formation rate can occasionally increase, on time scales of the order of $10^5 - 10^6$ yrs, the star formation rate will be inhibited and the cloud fragments. The cooling time of the environment within which the cloud is embedded is however very long: thus, star formation from the fragmented cloud remains strongly inhibited.

Key words: Galaxies: active – intergalactic Medium – large-scale structure of the Universe – methods: numerical.

1 INTRODUCTION

One of the most intriguing research areas in contemporary extragalactic astrophysics involves the study of the interplay between nuclear Black Holes (BHs) in galaxies, the (relativistic) jets which they can produce, and the Interstellar/Intergalactic Medium (ISM/IGM) within which they propagate. Observation and modeling of the propagation of jets within the ISM is an important part of this effort.

Since the seminal works of Scheuer (1974) and Falle (1991), much effort has been dedicated to the study of the propagation of a jet into the Interstellar Medium (hereafter ISM), and to its consequences for the detectability of the

jet. Relatively less attention has been paid to the impact of the jet and the cocoon generated by it on an inhomogeneous ISM. Saxton et al. (2005) have performed numerical simulations of the interaction of a cocoon with a set of clouds embedded within a diffuse ISM, mostly paying attention to the evolution of the jet's morphology. More recently, Krause & Alexander (2007, hereafter KA07) have also studied the turbulence induced by the interaction of jets with cold clouds embedded in an Interstellar/Intergalactic medium. In their simulations, they show that the jet is Kelvin-Helmholtz unstable, and can shear a cold cloud embedded in the ISM/IGM, thus inducing turbulence. Their simulation setup is however different from ours, mainly because they focus their attention on a small portion of the jet to study in detail the interaction with

* van@astro.ox.ac.uk

IGM clouds and the resulting turbulence. However, as we see in our simulations, turbulence in the cocoon arises naturally due to the general dynamical expansion of the cocoon itself. Sutherland & Bicknell (2007c,a) have taken into account the presence of large-scale density gradients in the ISM distribution, and the ability of a jet to emerge out of a galactic disc. They notice that the jet can eventually percolate through the inhomogeneous ISM, and emerges with a very disturbed morphology.

All the papers quoted made use of fixed-mesh numerical codes: in this paper, we use an Adaptive Mesh Refinement (AMR) code to follow in detail the evolution of turbulence within the cocoon produced by the jet during its propagation within the ISM/IGM. Allowing for a high refinement level, we can resolve small turbulent eddies, and study their statistical properties, and how they affect the evolution of a cloud embedded within the cocoon. We focus our attention on star formation within the cloud, and on the evolution of the density field within the cocoon, as our main aim is to understand how, within the turbulent cocoon produced by typical AGN jets at moderately high redshifts ($z \approx 1 - 2$), this turbulence can modify the ongoing star formation within the cloud.

The paper is organized as follows. In section 2 we briefly describe the numerical and computational set-up. In section 2, we present the numerical techniques and physical ingredients to simulate the jet and the ISM. We continue in section 3 by presenting the initial configuration and the physical parameters space spanned by the simulation, and we also discuss issues of numerical resolution. In section 5 we describe the results of the simulations and the evolution of the cocoon. We consider the evolution during both the *active* phase, while the jet is present, and the subsequent *passive* phase. Then, in section 6, we discuss the density probability distribution function (PDF) of the matter within the cocoon, and we find that it is well described by a modified lognormal function. In section 7 we then study the evolution of the Star Formation rate (SFR) within the cloud. In section 8 we discuss the implications of these simulations, comparing our results with those of similar papers. Conclusions are presented in the final section.

In the following, we adopt cgs units, unless otherwise explicitly stated, but we adopt kpc for lengths. The underlying cosmological parameters are taken from the 3-year WMAP best fit Λ CDM model (Bean 2006): $H_0 = 74_{-3}^{+3}$ Km/sec/Mpc, $\Omega_m = 0.234 \pm 0.035$, $\Omega_b h^2 = 0.0223 \pm 0.0008$. The unit of time is taken to be the Hubble time for this model, i.e.: $t_0 = 1.35 \times 10^{10}$ years. G , k_b and m_p denote the gravitational constant, the Boltzmann constant and the proton mass, respectively.¹

2 COMPUTATIONAL FRAMEWORK

To perform the simulations described here, we have used FLASH v. 2.5 (Fryxell et al. 2000), a parallel, Adaptive Mesh Refinement code which implements a second order,

shock-capturing PPM solver. FLASH's modular structure allows the inclusion of physical effects like external heating, radiative cooling and thermal conduction (among others). The user is permitted considerable freedom in the specification of the refinement criteria, which can be customized to reach very high spatial and temporal resolutions in selected regions.

The main purpose of this work is to study in detail the interaction of a relativistic jet and the cocoon which it generates with pre-existing clouds, and how it can affect star formation within the cloud itself. Ideally, a full 3D simulation should have a spatial resolution high enough to resolve *both* the turbulent motions within the cocoon and the thermodynamic structure of the cloud, until the end of the simulation. The former task is important when one realizes that, in addition to the direct interaction with the jet, the cloud is also significantly affected by the random interactions with the turbulent eddies present within the cocoon. The computational requirements imposed by this task, however, are prohibitive, when one considers that the smallest turbulent cells to be resolved should have a size comparable to that of the cloud ($10 h^{-1} pc$ here), and the computational box is between 2 and 4×10^2 times larger. For this reason, we have restricted ourselves to 2D simulations, where this resolution can easily be reached.

We have included radiative cooling, described by a standard cooling function with half solar metallicity (Sutherland & Dopita 1993), extended to high temperatures ($T > 10^7$ K, see appendix B). Gravity is also included, while thermal conduction and magnetic fields are not. The former could possibly be relevant for the evolution of the cocoon, although on timescales longer than those considered here (Krause & Alexander 2007). Regarding magnetic fields, the evidence is that, if present within the diffuse IGM, their magnitude is not larger than a few microgauss, thus making the IGM a high- β plasma, and the magnetic field would then not significantly affect the global dynamical evolution.

In the simulations the jet is modeled as a one-component fluid, with a density ρ_{jet} which is a fixed ratio ϵ_j of the environmental density ρ_{env} . In order to suppress the growth of numerical instabilities at the jet/IGM injection interface, we adopt a steep, but continuous and differentiable transverse velocity and density profile previously adopted in simulations of jet propagation (Bodo et al. 1994; Perucho et al. 2004, 2005):

$$v_{x,j} = \frac{V_j}{\cosh \{(y - y_j)^{\alpha_j}\}} \quad (1)$$

$$n_j = n_{env} - \frac{(n_{env} - n_j)}{\cosh \{(y - y_j)^{\alpha_j}\}} \quad (2)$$

where: $\alpha_j = 10$ is an exponent which determines the steepness of the injection profile and n_j, n_{env} denote the jet and environment number densities. This initial profile is highly sheared, and peaks around y_j , with most of the thrust $n_{jet} v_{jet}^2$ concentrated around the center of the profile. The presence of a highly sheared injection profile forces the code to refine the grid structure, populating the injection region with subgrid meshes, thus preventing the formation of numerical contact instabilities. In all our runs, the injection point of the jet is chosen to lie at the midpoint of the left boundary.

¹ For the interested reader, we have put some animations of these simulations on the website: http://web.ct.astro.it/cosmoct/web_group/research.html.

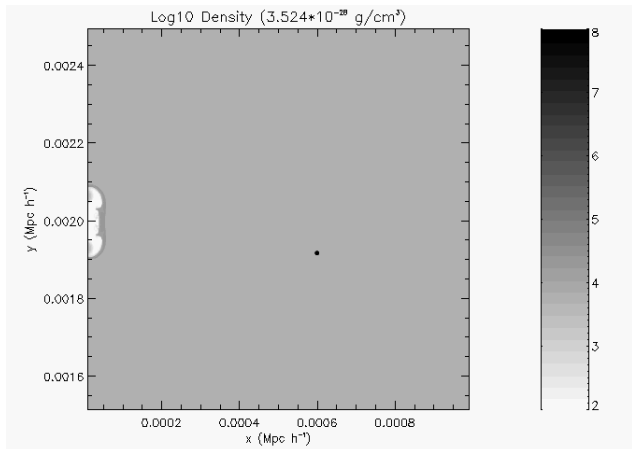


Figure 1. Initial configuration for the runs. The plot is a magnification of the actual simulation box, showing a small region of the larger simulation box. The small, dense cloud lying along the path of the jet, placed at (0.6, 1.92) (in $\text{kpc } h^{-1}$).

3 SIMULATIONS

Our simulations are characterized by seven parameters. Two of these characterize the diffuse ISM: n_{env} , T_{env} , two more the cloud: r_{cl} , M_{cl} , and finally three characterize the jet: n_j , y_j , V_j . As the SFR is mostly determined by the strength of the shock within the cloud, as previous models seem to suggest (Klein et al. 1994), we have decided to mostly vary the jet’s input power $P_{jet} = 0.5A_j m_H n_j V_j^3$ which, together with the density contrast, determines the timescale of the cloud’s disruption. We keep most of the other parameters fixed: ISM density and temperature at $1 \text{ e}^{-}\text{cm}^{-3}$ and 10^7 K , respectively, typical of the hot ISM in the central parts of a massive elliptical at high redshift ($z \approx 1$). Only in one run we have increased the size of the box, in order to check that the main features of the evolution do not depend on boundary conditions. All runs except one have been performed on a relatively small box ($4 h^{-1} \text{ kpc}$), while in run H2 we have used a box twice as large.

In Table 1 we summarize the main parameters of the different runs. The ratio between jet and environment density, n_j/n_{env} is fixed to 2×10^{-2} in runs using small boxes, and decreased to a slightly lower value (10^{-2}) in run H2. The injection region has a width of $100 h^{-1} \text{ pc}$ in runs in the small box, and twice as much in run H2. The parameter V_j in eq. 1, is computed once ρ_j , d_j and P_{jet} are assigned. Finally, we have chosen *open* boundary conditions, so the gas is free to flow out of the simulation box. The implication of this is that gas is not allowed to re-enter the box, so circulation motions on scales larger than the simulation box cannot be reproduced.

3.1 Initial configuration

We place a small, dense cloud at a position slightly offset from the jet’s propagation direction (see Fig. 1 and Table 3.1). In order to keep the same spatial resolution, the radius of the cloud is doubled in run H2, where the simulation box is larger: consequently also the initial mass of the

cloud is larger. We have chosen to study the effect of the jet on a cloud located very near to its path, because this allows us to check to what extent star formation is affected by the jet under the most extreme conditions. In a forthcoming paper we will study a more realistic setup, where we distribute a set of clouds with a realistic mass spectrum, and study how star formation changes according to the relative position within the cocoon associated with the jet.

Most of the runs were evolved up to $\approx 10^7$ yrs., while the jet was active and supplying energy to the cocoon. Only in one run (H4) the jet was switched off after 10^7 yrs., and the further evolution of the system was followed until the cloud was completely destroyed.

3.1.1 Model of embedded cloud

We have chosen a model for the structure of the embedded clouds suggested by the numerical simulations performed by Baek et al. (2005), because the physical ingredients of these simulations are likely to be representative of the physical processes present in the ISM/IGM. These simulations have been devised to provide a reasonable model for clouds embedded within the IGM. Different sources of heating (UV-background, the wind and radiative flux from the central QSO itself) provide a significant energy input which can promote the formation of pressure-confined clouds through thermal instability. Baek et al. (2005) have shown that, for typical IGM density and temperatures, similar to those considered in the present paper, the cooling time is a small fraction of the dynamical time, and the ISM is prone to the development of small, pressure-confined clouds. These are almost isothermal, with temperatures near the lower extreme of the cooling function ($T_{cl} \approx 10^4 \text{ K}$). In the mass range $10^{2.5} \leq M_{cl} \leq 10^7 M_{\odot}$ they find a relationship between r_t and the total mass M_{cl} :

$$r_t = \lambda M_{cl,4}^{\beta} \quad (3)$$

where we have defined: $M_{cl,4} = M_{cl}/10^4 M_{\odot}$. If r_t is measured in pc, we obtain: $\lambda = 28.87$, $\beta = 0.28 \pm 0.04$. The upper limit of this mass range corresponds to the Jeans mass for these clouds, implying that they are *not self-gravitating*.

As we show in Appendix A, a reasonable model for these clouds is the *Truncated Isothermal Sphere* (TIS Shapiro et al. 1999). Given the cloud’s mass M_{cl} , the final parameters of the configuration will depend on the background ISM thermodynamic state, and we assume that the latter is described by an unperturbed ideal equation of state with density and temperature ρ_{cl} and T_{cl} , respectively, as appropriate to a high temperature, low density, fully ionized plasma (e.g. Priest 1987). We denote the solution of the TIS equation by $F(\zeta)$, so that the cloud density can be written as: $\rho_{cl} = \rho_0 F(\zeta)$, ρ_0 being the normalization factor and $\zeta = r/r_0$ a normalized distance. The cloud’s structure is entirely specified by assigning r_0 , ρ_0 and the truncation distance r_t . Once the latter is determined by the radius-mass relation found by Shapiro et al. (1999), the two remaining factors are determined by imposing pressure equilibrium with the IGM, as shown in Appendix A.

Table 1. Parameters of the simulation runs. Columns from left to right are as follows: run label, simulation box size, background density (runs H1-3) or central density (runs NFW), jet/background density ratio, jet power.

run	L_{box} (kpc h^{-1})	n_{env} (cm $^{-3}$)	n_{jet}/n_{env}	W_{jet} (erg/sec)
H0	4	1	0.02	4×10^{40}
H1	4	1	0.02	8.61×10^{41}
H2	8	1	0.01	1.34×10^{44}
H3	4	1	0.02	10^{45}
H4	4	1	0.02	10^{46}

Table 2. Cloud parameters. All distances are expressed in kpc h^{-1} . From left to right, columns are as follows: simulation box size, x and y coordinates, cloud's radius and mass, the latter in M_{\odot} .

L_{box} (kpc h^{-1})	x	y	r_{cl}	M_{cl}
4	0.6	1.92	10	1.65×10^8
8	1.2	3.84	20	1.30×10^9

4 STAR FORMATION

Although our maximum spatial resolution could allow us to resolve subparsec scales, we cannot follow star formation in any detail, because this would require the inclusion of more physics (for instance a very detailed treatment of molecular cooling) and temporal resolution a few orders of magnitude higher than the one we have adopted. Instead, we assume that the cloud is converting gas into stars at a rate determined by the Schmidt-Kennicutt law (Schmidt 1963, 1959; Kennicutt 1998): $\dot{\Sigma} = A\Sigma^n$, with: $A = (2.5 \pm 0.17) \times 10^{-4} M_{\odot} yr^{-1} kpc^{-2}$, $n = 1.4 \pm 0.15$. At any time, we assume that star formation proceeds only within those regions of the simulation volume where the following criteria are satisfied:

- (i) Mass is larger than the Bonnor-Ebert mass;
- (ii) Temperature is less than a prescribed upper cutoff, i.e. we assume that star formation is sharply inhibited in regions having $T \geq T_c = 1.2 \times 10^4 K$.

The Bonnor-Ebert mass (Ebert 1955; Bonnor 1956) is defined as the largest mass which a pressure confined, gravitating cloud can reach before becoming unstable:

$$M_{be} = 1.18 \frac{c_s^4}{\sqrt{G^3 p_{ext}}} = 23.55 \frac{T_4^2}{p_{ext}^{1/2}} M_{\odot} \quad (4)$$

where p_{ext} is the pressure at the surface of the cloud, temperature is expressed in units of $10^4 K$, and we have assumed that an isothermal equation of state applies, so that the sound speed is given by: $c_s = (k_B T / m_p)^{1/2}$. The temperature cutoff is often adopted in star formation models to exclude regions where the UV flux would be too high to permit significant star formation. Our criteria to select the star forming region are very similar to those adopted by Schaye & Dalla Vecchia (2008).

From now on, all characteristic properties of the cloud such as its mass or size will always be referred to the *star forming region* as just defined.

4.1 Numerical resolution

As our main goal is that of studying in detail the evolution of star formation within the cloud, we need sufficiently high spatial resolution during each run. The outer parts of the cloud are stripped due to interaction with the jet, and it is in principle difficult to predict how much the cloud's size and mass will be reduced during the evolution. For this reason, we have applied a refinement criterion which will enable us to get high resolution even during the late phases, when the star forming region is considerably reduced. The spatial resolution in FLASH is determined by three parameters: the number of blocks in the initial decomposition, which in 2D simulations is given by: $N_{blx} \times N_{bly}$, the number of mesh cells within each block, $n_{bx} \times n_{by}$, and the maximum allowed refinement level l_r . In the present work we have chosen: $N_{blx} = N_{bly} = 20$, $n_{bx} = n_{by} = 8$, and $l_r = 6$. Thus, the smallest spatially resolved scale (down to mesh level) along each direction is given by: $\Delta_x = \Delta_y = (L_{box}/N_{blx}) / (2^{(l_r-1)} n_{bx})$, which, for $L_{box} = 4h^{-1} kpc$ gives: $\Delta_x = 0.78125 h^{-1} pc$. Note that the maximum refinement level around the cloud is reached already at the start of the simulation, because of the refinement criterion adopted. The approximate number of mesh cells contained within a cloud of radius R_{cl} , n_m , can be estimated as: $n_m = int(\pi R_{cl}^2 / \Delta A_m)$, where $\Delta A_m = \Delta_x \Delta_y$ is the area of a single mesh. In our case initially $R_{cl} \simeq 10h^{-1} pc$, so we get: $n_m \approx 514$. A typical block distribution is shown in Figure 2.

By default, FLASH refines the grid at those points where one of the components of the second spatial derivative of some user-selected quantities, normalized to the square of the spatial gradient, exceeds some pre-established threshold value. The quantities we check for refinement are density, pressure and temperature. This default criterion is sufficient to resolve the highly compressed regions on the scale of the clouds we are interested in, so we do not add any additional, customized refinement criterion.

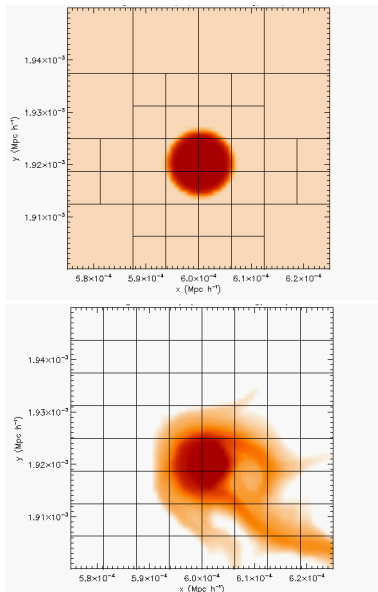


Figure 2. Computational block distribution for two different steps of run H1, taken at $t = 2.6 \times 10^5$, *upper* and 5.3248×10^5 , *lower* (time in yrs). Each little square represents a FLASH block, and each of these contains 64 mesh cells (not reproduced in the figures). Note that the size of the region is $50 h^{-1}$ pc, a small fraction of L_{box} , and the blocks represented are at the highest refinement level.

5 EVOLUTION OF THE COCOON

The injection of energy into the ISM/IGM can engender turbulence, mostly because the jet is supersonic at and near the injection point. Most previous work aimed at describing the general structure and evolution of the cocoon, however, has paid more attention to the global dynamics of the cocoon. Turbulence can have a significant impact on the evolution of the embedded clouds, and for this reason we study it in more detail in the next sections.

5.1 Active phase: evolution during jet injection

Soon after the jet enters the ISM/IGM a cavity forms, and the gas which has been swept out piles up into a transition layer. In Figure 3 we show an output of one of the runs at a rather advanced stage. We can easily distinguish an internal low-density, high temperature *cocoon* and a *shocked ambient gas* region, externally bounded by a tangential discontinuity with the outer ISM/IGM. One of the most interesting features we find is that these regions are also *dynamically* very different. The region containing the shocked gas is threaded by a series of weak transonic shocks, and it has on average an expansion motion, while in the cocoon a large-scale circulation parallel and opposite to the main stream of the jet develops, originating from gas reflected away from the region near the hot spot. This circulation produces shear motions which then decay into weak turbulence within the cocoon. Pre-existing clouds embedded within the ISM/IGM are heavily affected by this turbulence. The typical velocities of these shearing motions are large but, due to the very high temperatures within the cocoon ($T \approx 10^9 - 10^{11}$ K), they are only moderately transonic.

As one can notice by inspecting Figure 4, the pressure within the cocoon can reach high values, because the temperatures are on average very high. Also the region around the terminal part of the jet, near the hot-spot, is subjected to high pressures, which increase steadily until the cocoon’s expansion is halted by the ram pressure. We notice that the highest values of pressure are attained within the *shocked ambient gas region*, mostly driven by the higher density, up to 3 orders of magnitude larger than the average density in the cocoon. The Mach number is higher near the jet, particularly near the injection point, but in the overall region (cocoon and *shocked gas layer*) it never reaches values larger than $\mathcal{M} \approx 3 - 3.5$. The dynamical evolution of the hot spot, i.e. the region between the tip of the jet and the terminal part of the cocoon, is quite interesting. Here, however, we will concentrate on those features more directly related to the interaction with clouds, leaving to further work a more detailed analysis of the features of interest relevant to the modeling of the radio jet.

5.2 Passive evolution

All runs were stopped when the jet was still active, except for run H4, which was continued for about 5×10^6 yrs. after the jet was switched off. This time was chosen to be $t \approx 10^7$ yrs., within the range of a typical duty cycle for the AGN. The cocoon expands up to a maximum radius determined by the jet power and the environmental ram pressure. When the duty cycle of the AGN is completed, the jet injected power decreases very rapidly, and the cocoon is not anymore fed by the jet. The evolution is mostly driven by inertial motions: a snapshot is shown in Figure 5. The typical velocities are still quite high within the cocoon, but the expansion of the shocked ambient gas region has already been slowed down by the ISM/IGM ram pressure, and it is now decelerating, while slowly expanding. Notice that the cloud is threaded by arc-like internal shocks within the cloud (Figure 7, *left*), previously noticed in similar simulations of shock-cloud interactions (Nakamura et al. 2006).

The further evolution of the cloud during the passive phase shows some features not emphasized in previous papers. A continuous, decelerating flow now takes place within the cocoon, primarily driven by the inertial motions, because at the typical densities of the cocoon ($n_e \approx 10^{-4} - 10^{-2} \text{ cm}^{-3}$) the gravitational pull is less than the inertial force. A zero total velocity line now separates the cocoon from the external ISM. In the latter the decelerating, outward directed expansion motion changes to a wind as the plasma leaks out of the simulation box and the density decreases. A similar motion, but directed in the opposite direction, drives the gas past the left vertical boundary, i.e. towards the AGN and the galaxy bulge, increasing the density within this region. As a consequence of the generalized density decrease, the cooling time increases even further, although it was already much larger than the free fall time-scale.

This back-flow within the cocoon has some interesting consequences for the embedded clouds. During the active phase, the cloud was already subject to a significant compression from the turbulent motions, and, as a consequence, its density had also risen. Its temperature was however typically higher than $5 \times 10^5 - 10^6$ K, a level maintained mostly by the turbulent dissipation. However, during the passive

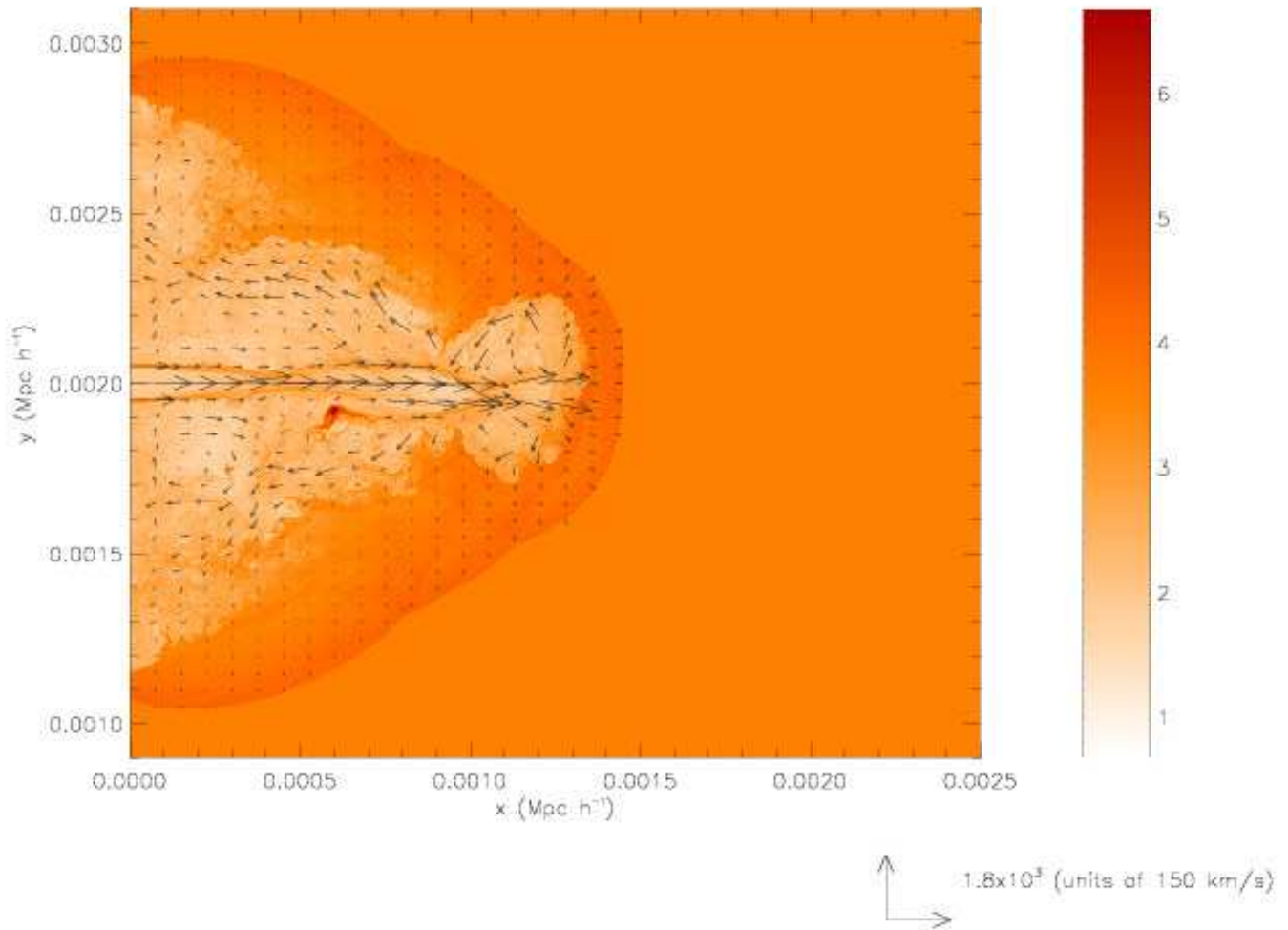


Figure 3. Density and velocity distribution at $t = 8.1 \times 10^4$ yrs. for run H4. The logarithmic density scale ranges from 10^{-3} to 10^3 $e^- \text{ cm}^{-3}$. The transition region between the cocoon and the external medium is threaded by a series of transonic shock waves (*shocked ambient gas layer*). The high-density enhancement within the cocoon originates out of the stripped material from a cloud initially set near $(0.6, 1.92) h^{-1}$ kpc, which has been shocked by the jet.

phase, the cloud is embedded within a continuous decelerating stream, which is now more laminar than turbulent (Figure 6). This flow continues to compress the cloud, which cools efficiently: its average density also increases, and its temperature decreases, a trend which can be clearly seen on the right hand side of figure 7. On a longer time scale the cloud eventually is completely stripped, due to KH instabilities. Our simulations do not have the spatial and temporal resolution to further follow the fragmentation of this cloud, which will be treated in a separate paper. The overall action of the cloud's compression during the *active* jet phase, and of the cooling and further compression during the passive phase, can result into an occasional enhancement of the region of the cloud where favorable conditions for star formation are possible, as can be seen from figure 7. The gas stripped away by KH instabilities from the cloud tends to

form filamentary, high density structures, where temperatures can reach high values ($T \sim 10^4 - 4 \times 10^5$ K). Star formation within these filaments, due to these high temperatures, is thus inhibited, and the cloud eventually is completely destroyed.

6 PROBABILITY DENSITY DISTRIBUTION

The cocoon represents for the cloud an environment radically different from the hot ISM: on average, temperatures are higher and densities lower, and it is also in a turbulent state, permeated by a series of turbulent eddies, which produce a random, intermittent series of stresses on the cloud. This scenario is more complex than those envisaged in previous models of cloud evolution under external shocks

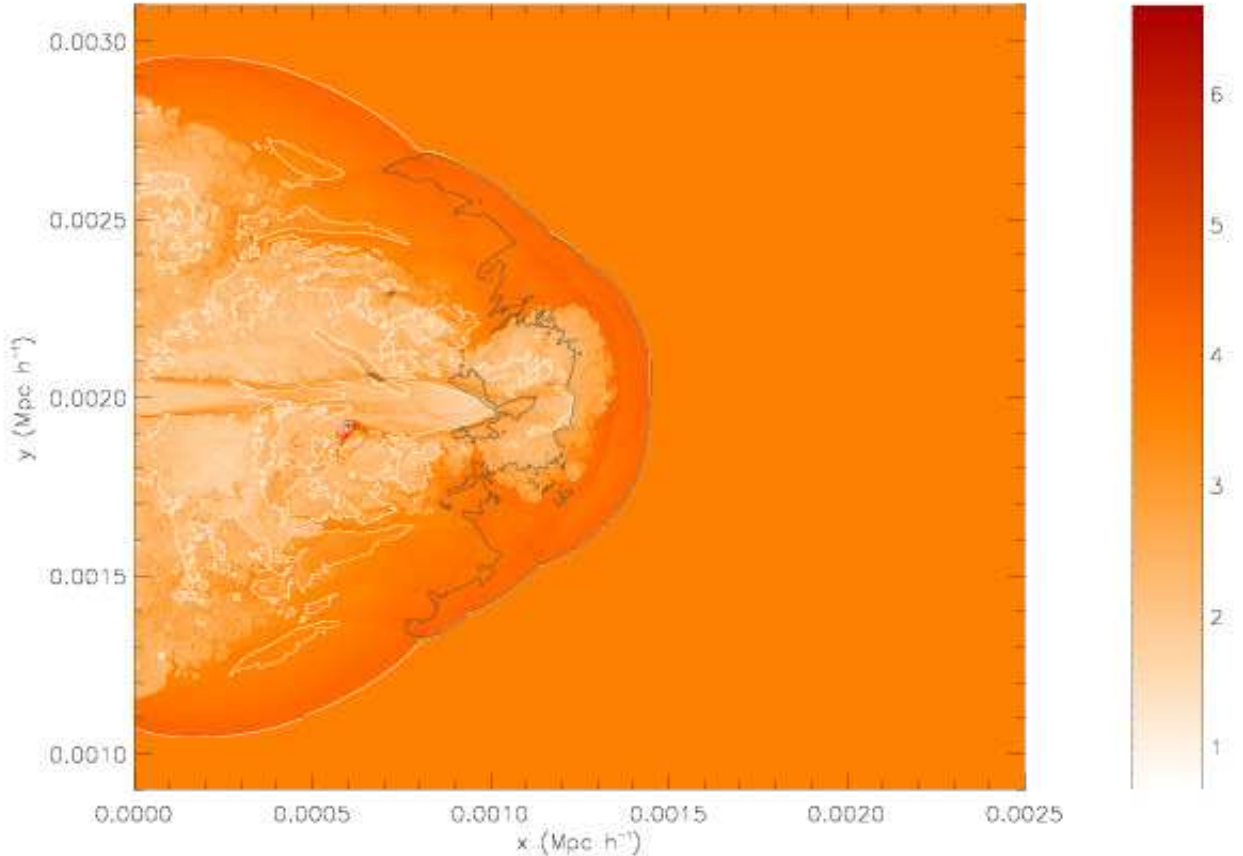


Figure 4. Density and pressure distribution for the same output of Figure 3. We show two pressure contours, corresponding to 5.77×10^9 (white) and 2.88×10^{10} (dark grey) $\text{K} \cdot \text{cm}^{-3}$.

(Klein et al. 1994; Nakamura et al. 2006), and a model of the turbulence within the cocoon is then a prerequisite to developing a model of the evolution of clouds within a turbulent environment. We will develop the latter in a following paper: here we will only consider the density PDF within the cocoon.

Simulations of turbulence in the ISM suggest that, on galactic scales, a lognormal Probability Distribution Function (LNPDF) provides a viable description of the distribution of density fluctuations over a large range of densities typical of galactic ISM (e.g. Padoan et al. 1997; Wada & Norman 2007, 2001). The physical conditions of the system considered in this work, however, are very different from those typical of the galactic ISM, where temperatures are considerably lower ($T \approx 10 - 10^2$ K) and densities higher, so we do not expect *a priori* to find the same PDF. Moreover the presence of the jet, which injects energy and momentum into an expanding cocoon, results in a *non-stationary* back-

ground. In Figure 8 we show the evolution of the density PDF for one of the runs (H4). One notices that the PDF is bimodal, with two peaks at densities respectively lower and higher than the initial ambient density ($n_e = 1 \text{ cm}^{-3}$). These two peaks correspond to two spatially separated regions: the low density distribution arises predominantly within the cocoon, while the high density component is associated with the gas in the shocked gas region. The continuous and dotted curves are two least-square fits of the low-density PDF, with two different fitting functions: an exponentially truncated power law (continuous curve),

$$P_{tr} = A |x|^n \exp\left(-\frac{x}{b}\right) \quad (5)$$

and a modified lognormal (dotted curve):

$$P_{lm} = B \exp\left[-\frac{(x - \langle x \rangle)^2}{\sigma^2} - bx\right] \quad (6)$$

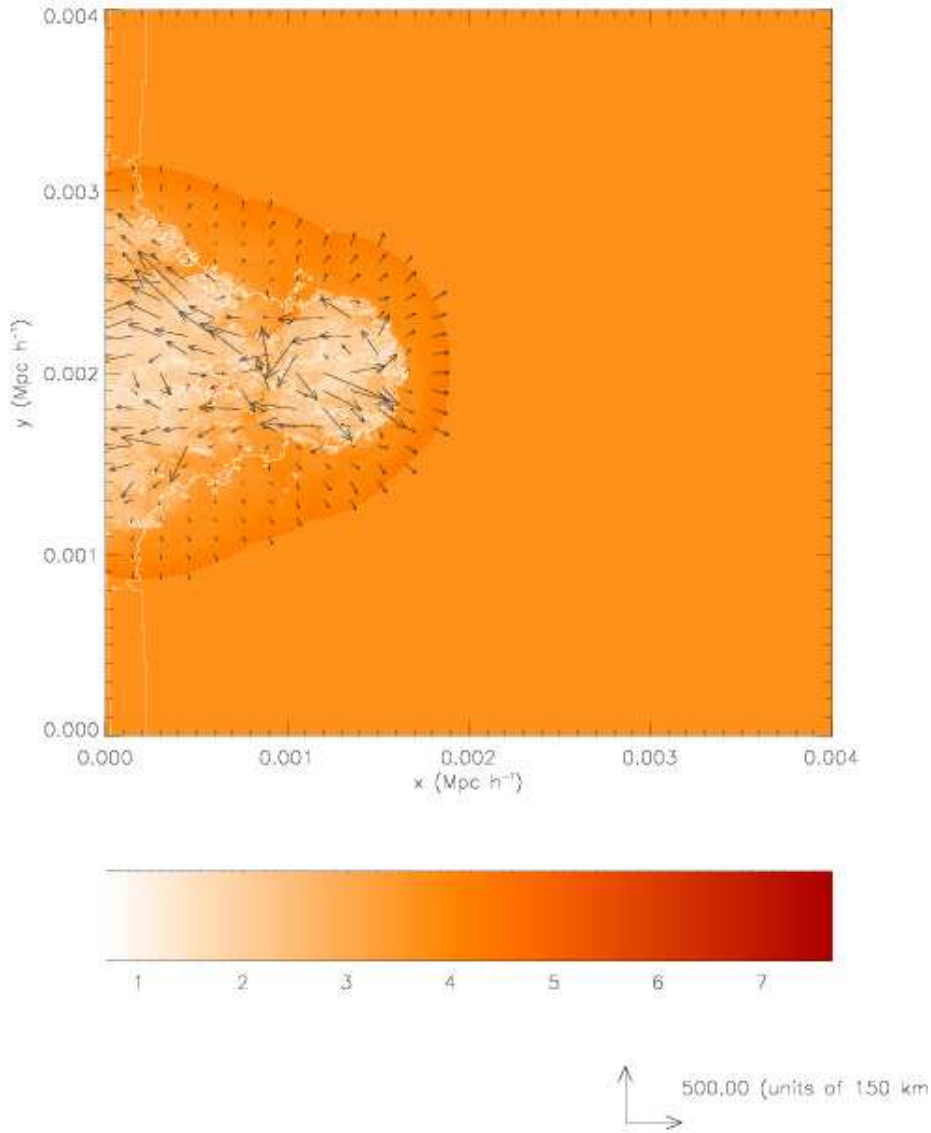


Figure 5. Density field of run H4 at $\Delta t = 2.45 \times 10^5$ yrs after the jet has been shut off (i.e. at a time $t = 1.00245 \times 10^7$ yrs since the beginning of the simulation). The cocoon and the tangential discontinuity are now dynamically very different, and their boundary is marked by a zero velocity contour.

where: $x = \text{Log}(\rho)$. The quality of the two fits is comparable: $\chi^2/d.o.f = 1.76$ (truncated power law) and $\chi^2/d.o.f = 1.32$ (modified lognormal). A modified lognormal distribution is generally expected in any fluid system whose density distribution is the result of a series of uncorrelated shocks (e.g. Vázquez-Semadeni 1994; Padoan et al. 1997; Passot & Vázquez-Semadeni 1998; Kritsuk et al. 2007). Such a PDF has also been found in simulations of turbulence and global star formation in galactic discs (Wada & Norman 2001; Tasker & Bryan 2006; Wada & Norman 2007), thus

suggesting that it could also arise in stationary systems where turbulence is not only artificially forced within the simulation box. Note that in the model of Passot & Vázquez-Semadeni (1998) this particular form for the PDF should be independent of the dimensionality of the system, although the parameters characterizing the distribution will depend on it. It seems reasonable to assume that the main driver of this weak turbulence are multiple shocks within the cocoon, forming initially from the evolution of Kelvin-Helmholtz instabilities at the jet-ISM inter-

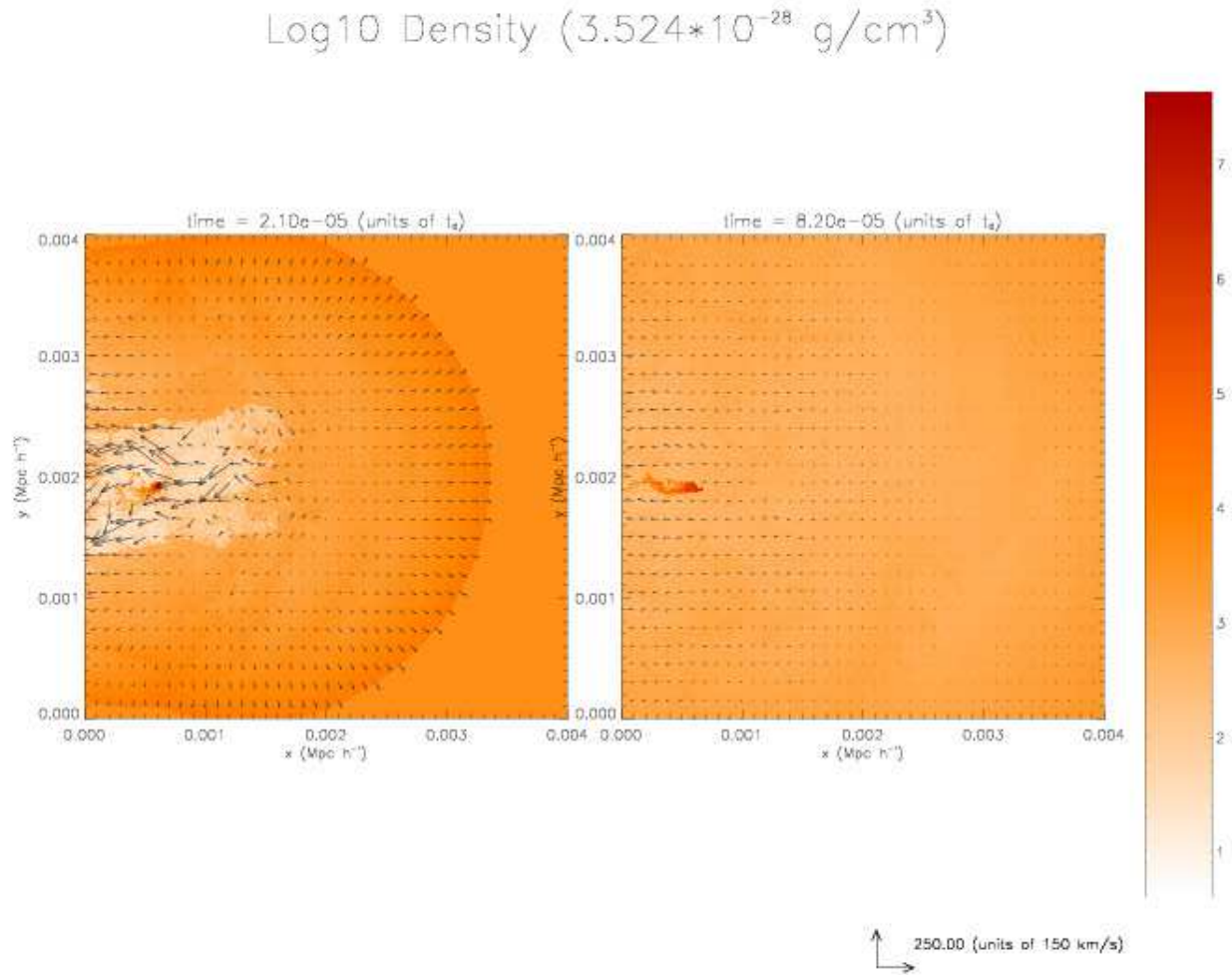


Figure 6. Density evolution at two different epochs after the jet has been switched off. The system evolves towards homogeneity and equilibrium on a temporal scale mostly determined by the decay of the inertial motions. Time is measured in units of Hubble time t_0 , so the plot on the left is at an epoch $t = 2.835 \times 10^5$ yrs., and the one on the right plot for $t = 1.107 \times 10^6$ yrs.

face. These shocks then propagate within the cocoon, and are reflected at the internal interface with the shocked gas region.

7 EVOLUTION OF STAR FORMATION RATE

The influence of the jet/cocoon on star formation within the cloud is the result of the competition between different physical factors. The impact of the shock and the increased pressure within the cocoon result in a overall compression of the cloud, which tends to *increase* its density and specific star formation rate. On the other hand, the increase of temperature and stripping of the outer regions due to KH and other instabilities tend to reduce the mass of the cloud, thus contributing to a *decrease* of the global star formation rate. The detailed temporal evolution of the cloud is governed by the turbulence within the cocoon, and subsequently by the evolution of the back-flow. In Figure 9 we show the evolution of the *specific* and *global* star formation rates during the active phase, when the jet is still feeding energy into the cocoon. One notices that in runs H0-H2 the specific SFR oc-

asionally increases, due to the increase of the average density of the star forming region. The *global* SFR also shows similar fluctuations, although of smaller amplitude, in all these runs. A similar trend is observed for the evolution of the mass of the star forming region, Figure 10: some episodic increases are seen, in temporal and sign correspondence with the fluctuations of the SFRs. However, stripping tends to diminish the mass of the cloud, so we are forced to conclude that these episodic increase of the star-forming region can only be attributed to occasional cooling, driven by thermal instability. This gas is however soon warmed up again by the warm, turbulent environment of the cocoon, and the SFR then decreases.

A similar trend is observed in run H4, during the passive phase. We have already seen from Figure 7 that the cloud, exposed to the back-flow from the jet, becomes more filamentary and cold. However, we see from Figure 11 that its mass decreases dramatically, because the inner cold regions become less dense, and consequently both the specific and the global SFRs diminish. We can thus conclude that, in general, the interaction with the jet/cocoon tends to inhibit in the long term star formation within the cloud. This

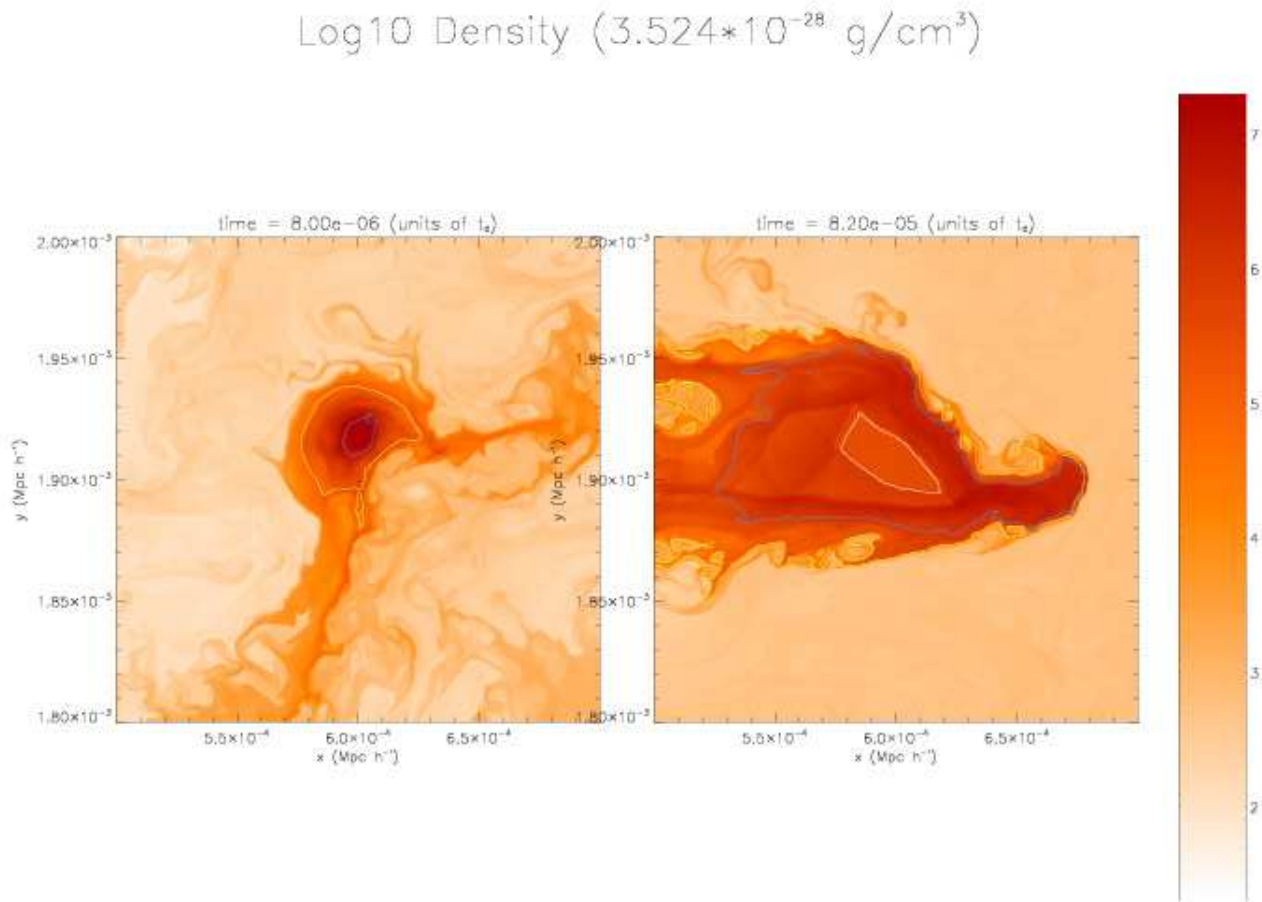


Figure 7. Evolution of density and temperature in the compressed cloud, during the active phase (*left*), during the which the jet is feeding energy into the cocoon, and some time after it has been switched off (*right*). The contours superimposed on the density maps trace regions of equal temperature, and correspond (from the inner- to the outermost contour) to the following temperatures: $T = 10^4, 10^7$ and 10^9 K.

suppression however is not continuous, but seems rather to proceed in an intermittent way, and is interrupted by short episodes during which the SFR occasionally increases. This trend seems to continue during the passive phase, when the cloud is completely stripped and its SFR decreases rapidly.

8 DISCUSSION

Some features of the evolution of the clouds described in this work have been previously found in earlier work. Our initial setup is very similar to that used by Mellema et al. (2002): the initial temperatures of the ISM and clouds are the same, and our clouds are also in pressure equilibrium with the diffuse phase. We also find that the stripped cloud seems to fragment into filamentary structures, whose density and specific SFR seem to occasionally increase. Although these structures seem to persist, we have shown that their global star formation rate tends to decrease.

Recent observational evidence suggests the star formation history in early-type galaxies can be more complex than in the standard, monolithic scheme. There is both evi-

dence of quenching of star formation (Kaviraj et al. 2007; Schawinski et al. 2006) and of recent star formation episodes (Sarzi et al. 2007; Kaviraj et al. 2007; Thomas et al. 2007; Yi et al. 2007): both could be induced by AGN activity. It is then important to understand the physical mechanism of jet-ISM interaction, and how star formation can be affected. The simulations we have presented in this work represent an attempt to introduce some realistic physical ingredients of the ISM structure into a numerical model, and to understand how these affect the evolution of SFR in the cloud.

There are some features which have not yet been included into this model. One is related to the quantitative relevance of this model. Although the duration and frequency of AGN jets are not well known (Blundell et al. 2002), typical estimates of the *active* phase of the jet range between $10^7 - 10^8$ yrs, comparable to those adopted in the simulations presented in the previous sections. Empirical evidence from modeling of SMBH feeding in the context of hierarchical structure formation suggests that the AGN phenomenon persists for several Gyr (Mahmood et al. 2005; Bromley et al. 2004; Haehnelt 2004), or many galaxy dynamical times. Hence AGNs are certainly capable of provid-

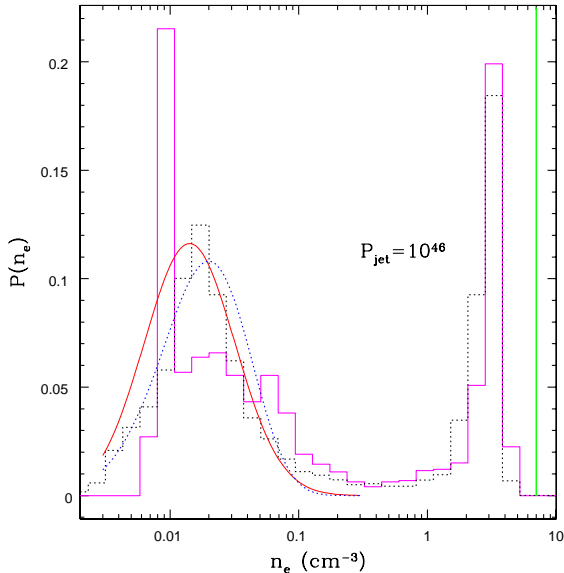


Figure 8. Density PDF for run H4. The analysis was performed only within the cocoon/shocked ambient gas region. The two histograms show the PDF at two different epochs: $t=1.35 \times 10^4$ yrs. (dotted), and $t=9.45 \times 10^4$ yrs. (continuous). The curves show two best fits for the latter epoch: an exponentially truncated power law *continuous* and a modified lognormal (*dotted*). The vertical line at $n_e = 7$ is the maximum density possible for fully radiative shocks (Bouquet et al. 2000). Best fit parameters are given by: $(A, b, n) = (1.141 \times 10^5, 14.486, 24.612)$ (eq. 5), and: $(B, \langle x \rangle, \sigma, b) = (3.66 \times 10^{-3}, -1.6, 0.498, 2.005)$ (see eqs. 5 and 6).

ing significant feedback over the time-scales relevant to star formation and gas accretion in hierarchical galaxy formation models.

Our simulations are restricted to only *one episode* of AGN activity: a further episode of jet injection would certainly propagate into a very hot and low-density ISM, because our simulations show that the diffuse ISM/IGM within the cocoon reaches very high temperatures ($T \approx 10^8 - 2 \times 10^{11}$ K) and low densities ($n_e \approx 10^{-2} - 10^{-1} \text{ cm}^{-3}$), depending on the initial temperature and on the jet power at the time of its maximum expansion. Under these conditions, the cooling time exceeds the dynamical time by a factor: $t_{cool}/t_{dyn} \approx 6.5 \times 10^2 - 3 \times 10^5$, thus the heated gas does not cool significantly (as already noted by Inoue & Sasaki 2001). Thus, a second jet would propagate into an environment where the ram pressure will be considerably higher, $p_{ism} \approx 10^6 - 2 \times 10^{10} \text{ Kcm}^{-3}$ (the initial pressure in the ISM was $p_{ism} = 10^7 \text{ k}^{-1}$), and would probably be quenched. We will verify these predictions in subsequent work.

Despite the very high temperature within the cocoon, as soon as the jet is switched off, we observe that the shocked clouds which are not evaporated are subject to a back-flow originating from the gas within the cocoon. As a consequence, they become filamentary, and their temperature decreases, but we have seen that the mass of the star-forming regions within the cloud also diminishes, so eventually the global SFR is reduced. In a subsequent paper, we will present results of a more realistic simulation where we consider the propagation of a jet into a *multicloud* system, and we will

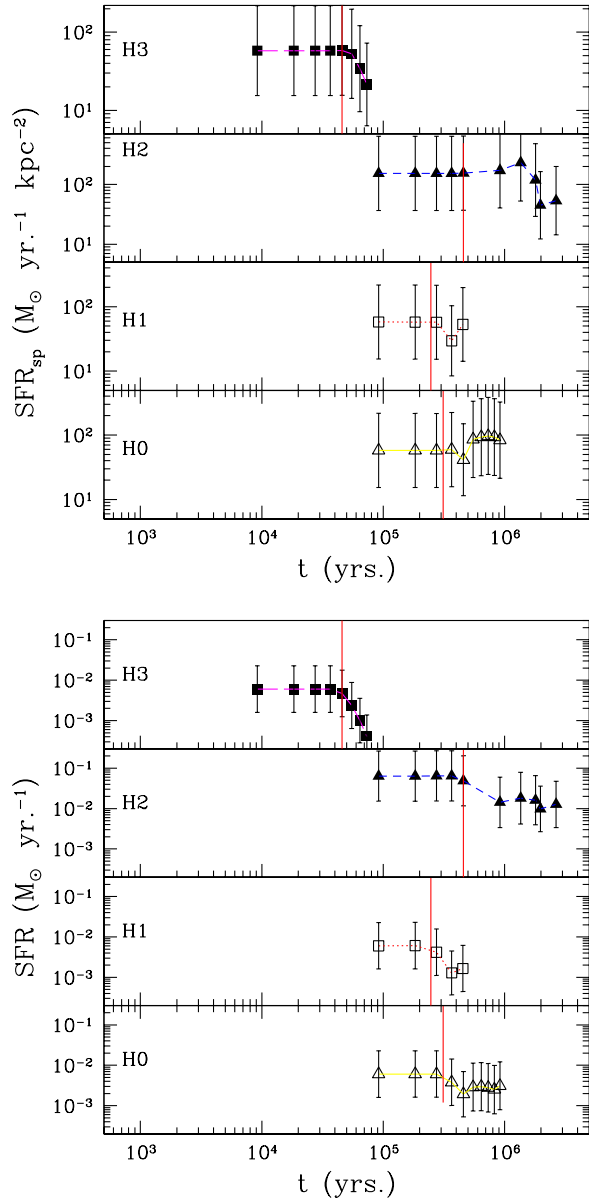


Figure 9. Evolution of the cloud's star formation. The red vertical bar labels the time when the jet/cocoon first hits the cloud. Error bars are computed from the $\pm 1\sigma$ errors of the Schmidt-Kennicutt law (Kennicutt 1998). *Upper plot*: Specific star formation rate, *lower plot*: Total star formation rate over the whole cloud.

then be able to address the problem of AGN feedback in a more quantitative, statistical fashion.

Our simulations differ significantly from those of KA07, because the turbulence within the cocoon surrounding the propagating jet is generated naturally by the interaction of the jet with the ISM/IGM, while KA07 studied the turbulence associated with the disruption of pre-existing ISM/IGM clouds due to Kelvin-Helmholtz instabilities at the jet-IGM interface. There are however some features which we have not addressed in our simulations. Sutherland & Bicknell (2007b) have simulated the propagation of a jet which first emerges out of a gaseous disc. They

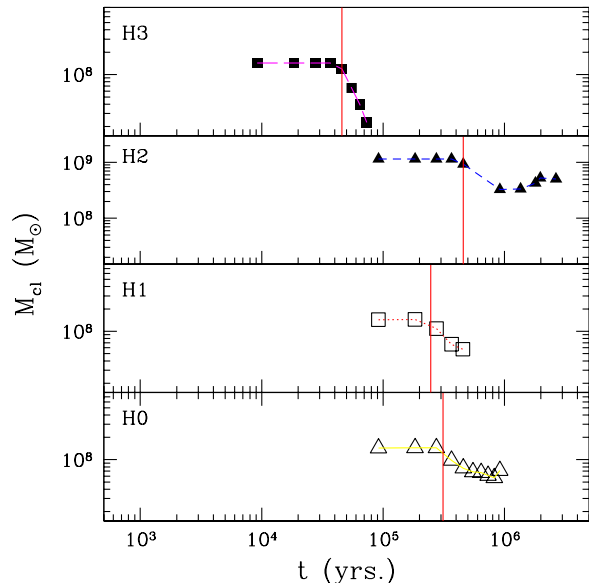


Figure 10. Evolution of the mass of the cloud’s star-forming region.

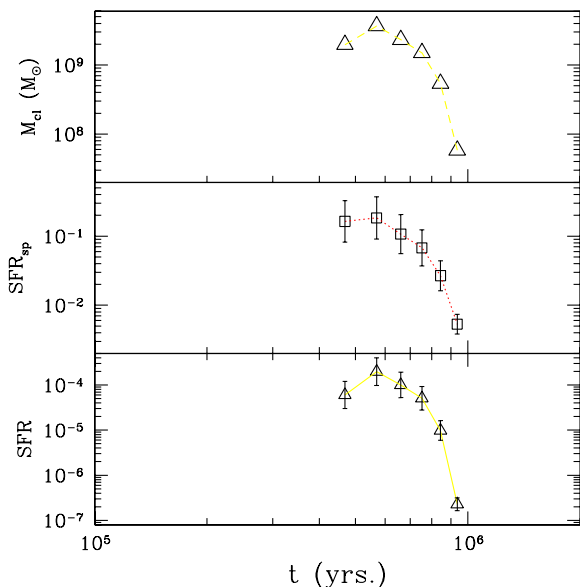


Figure 11. Mass and SFR evolution after the switch off of the jet (run H4). Time is now measured in yrs. after the switch off epoch (arbitrarily fixed at $t=10^7$).

note that the disc has a strong effect on the energy budget of the jet and also on its morphology: during its initial propagation the jet percolates through the disc, and it needs more time to overcome this initial pressure and emerge out of the disc into the ISM. Sutherland & Bicknell do not consider the compression of pre-existing clouds: the main target of their work is a detailed study of the morphology of the emerging jet, and a comparison with observations. A significant gaseous component, often distributed in disc-like structures, seems however to be present in relevant amounts ($10^9 - 10^{10} M_{\odot}$) also in a fraction of early-type galaxies

(Combes et al. 2007; Morganti et al. 2006; Sarzi et al. 2007; Macchetto et al. 1996; Goudfrooij et al. 1994).

9 CONCLUSION

The simulations we have performed in this work have as a target the propagation of the jet into the inhomogeneous ISM of an host galaxy. We have restricted our interest to the central region of a model elliptical galaxy ($r < 4 h^{-1}$ kpc), and we have studied the propagation of the jet and its interaction with a single cloud. The adoption of an AMR code like FLASH has proved crucial for studying, in the same simulation, both the large-scale properties of the jet-ISM interaction and the interaction with a small cloud. We have modeled star formation within a small, dense cloud assuming that it follows the Schmidt-Kennicutt law, and we have studied how the SFR is modified by the impact of the jet/cocoon. In general, we find that the SFR could be occasionally enhanced, but in the long run the cloud is stripped by KH instabilities and its SFR decreases. After the jet has been switched off, a laminar back-flow flow develops which continues to compress and strip the cloud, until the latter loses a significant fraction of its mass. Due to the very long cooling time of the cocoon, the cloud is embedded in a very hot, low-density medium, and this eventually results in suppression of star formation. We note that our results are preliminary being restricted to simulations in 2D for a single cloud. In further work we will extend our study to full 3D simulations and to an inhomogeneous protogalaxy.

ACKNOWLEDGMENTS

The work of V.A.-D. has been supported by the European Commission, under the VI Framework Program for Research & Development, Action “*Transfer of Knowledge*” contract MTKD-CT-002995 (“*Cosmology and Computational Astrophysics at Catania Astrophysical Observatory*”). V.A.-D. would also express his gratitude to the staff of the sub-department of Astrophysics, Department of Physics, University of Oxford, and of the Beecroft Institute for Particle Astrophysics, for the kind hospitality during the completion of this work.

The software used in this work was partly developed by the DOE-supported ASC/Alliance Center for Astrophysical Thermonuclear Flashes at the University of Chicago. Finally, this work makes use of results produced by the PI2S2 Project managed by the Consorzio COMETA, a project co-funded by the Italian Ministry of University and Research (MIUR) within the *Piano Operativo Nazionale “Ricerca Scientifica, Sviluppo Tecnologico, Alta Formazione” (PON 2000-2006)*. More information is available at <http://www.pi2s2.it> (in italian) and <http://www.trigrad.it/pbeng/engineindex.php>.

REFERENCES

- Baek C. H., Kang H., Kim J., Ryu D., 2005, *ApJ*, 630, 689
- Bean R., 2006, *New Astronomy Review*, 50, 850
- Blundell K. M., Rawlings S., Willott C. J., Kassim N. E., Perley R., 2002, *New Astronomy Review*, 46, 75

Bodo G., Massaglia S., Ferrari A., Trussoni E., 1994, *A&A* , 283, 655
 Bonnor W. B., 1956, *MNRAS* , 116, 351
 Bouquet S., Teyssier R., Chieze J. P., 2000, *Astrop. J. Supp.* , 127, 245
 Bromley J. M., Somerville R. S., Fabian A. C., 2004, *MNRAS* , 350, 456
 Combes F., Young L. M., Bureau M., 2007, *MNRAS* , 377, 1795
 Ebert R., 1955, *Zeitschrift fur Astrophysik*, 37, 217
 Falle S. A. E. G., 1991, *MNRAS* , 250, 581
 Fryxell B., Olson K., Ricker P., Timmes F. X., Zingale M., Lamb D. Q., MacNeice P., Rosner R., Truran J. W., Tufo H., 2000, *Astrop. J. Supp.* , 131, 273
 Goudfrooij P., Hansen L., Jorgensen H. E., Norgaard-Nielsen H. U., 1994, *A&A Supp.* , 105, 341
 Haehnelt M. G., 2004, in Ho L. C., ed., *Coevolution of Black Holes and Galaxies Joint Formation of Supermassive Black Holes and Galaxies*. p. 405
 Inoue S., Sasaki S., 2001, *ApJ* , 562, 618
 Kaviraj S., Khochfar S., Schawinski K., Yi S. K., Gawiser E., Silk J., Virani S. N., Cardamone C., van Dokkum P. G., Urry C. M., 2007, *astro-ph/0709.0806*, 709
 Kaviraj S., Kirkby L. A., Silk J., Sarzi M., 2007, *astro-ph/0707.3570*, 707
 Kennicutt Jr. R. C., 1998, *ApJ* , 498, 541
 Klein R. I., McKee C. F., Colella P., 1994, *ApJ* , 420, 213
 Krause M., Alexander P., 2007, *MNRAS* , 376, 465
 Kritsuk A. G., Padoan P., Wagner R., Norman M. L., 2007, *astro-ph/0706.0739*, 706
 Macchetto F., Pastoriza M., Caon N., Sparks W. B., Gavalisco M., Bender R., Capaccioli M., 1996, *A&A Supp.* , 120, 463
 Mahmood A., Devriendt J. E. G., Silk J., 2005, *MNRAS* , 359, 1363
 McCrea W. H., 1957, *MNRAS* , 117, 562
 Mellema G., Kurk J. D., Röttgering H. J. A., 2002, *A&A* , 395, L13
 Morganti R., de Zeeuw P. T., Oosterloo T. A., McDermid R. M., Krajnović D., Cappellari M., Kenn F., Weijmans A., Sarzi M., 2006, *MNRAS* , 371, 157
 Nakamura F., McKee C. F., Klein R. I., Fisher R. T., 2006, *Astrop. J. Supp.* , 164, 477
 Padoan P., Jones B. J. T., Nordlund A. P., 1997, *ApJ* , 474, 730
 Park M.-G., Ostriker J. P., 2001, *ApJ* , 549, 100
 Passot T., Vázquez-Semadeni E., 1998, *Phys. Rev. E* , 58, 4501
 Perucho M., Hanasz M., Martí J. M., Sol H., 2004, *A&A* , 427, 415
 Perucho M., Martí J. M., Hanasz M., 2005, *A&A* , 443, 863
 Priest E. R., 1987, *Solar magneto-hydrodynamics*. by E.R. Priest. Dordrecht: D. Reidel, 1987.
 Sarzi M., Bacon R., Cappellari M., Davies R. L., Emsellem E., Falcon-Barroso J., Krajnovic D., Kuntschner H., McDermid R. M., Peletier R. F., de Zeeuw T., van de Ven G., 2007, *astro-ph/0709.1394*, 709
 Saxton C. J., Bicknell G. V., Sutherland R. S., Midgley S., 2005, *MNRAS* , 359, 781
 Schawinski K., Khochfar S., Kaviraj S., Yi S. K., Boselli A. e. a., 2006, *Nature* , 442, 888
 Schaye J., Dalla Vecchia C., 2008, *MNRAS* , 383, 1210

Scheuer P. A. G., 1974, *MNRAS* , 166, 513
 Schmidt M., 1959, *ApJ* , 129, 243
 Schmidt M., 1963, *ApJ* , 137, 758
 Shapiro P. R., Iliev I. T., Raga A. C., 1999, *MNRAS* , 307, 203
 Stepney S., Guilbert P. W., 1983, *MNRAS* , 204, 1269
 Sutherland R. S., Bicknell G. V., 2007a, *Ap&SS* , 311, 293
 Sutherland R. S., Bicknell G. V., 2007b, *astro-ph/0707.3668*, 707
 Sutherland R. S., Bicknell G. V., 2007c, *Astrop. J. Supp.* , 173, 37
 Sutherland R. S., Dopita M. A., 1993, *Astrop. J. Supp.* , 88, 253
 Svensson R., 1982, *ApJ* , 258, 335
 Tasker E. J., Bryan G. L., 2006, *ApJ* , 641, 878
 Thomas D., Maraston C., Schawinski K., Sarzi M., Joo S.-J., Kaviraj S., Yi S. K., 2007, in *IAU Symposium Vol. 241 of IAU Symposium, Environment and the epochs of galaxy formation in the SDSS era*. pp 546–550
 Vazquez-Semadeni E., 1994, *ApJ* , 423, 681
 Wada K., Norman C. A., 2001, *ApJ* , 547, 172
 Wada K., Norman C. A., 2007, *ApJ* , 660, 276
 Wolfe B., Melia F., 2006, *ApJ* , 637, 313
 Yi S. K., Kaviraj S., Schawinski K., 2007, in *Revista Mexicana de Astronomia y Astrofisica Conference Series Vol. 28 of Revista Mexicana de Astronomia y Astrofisica Conference Series, The Star Formation History of Early-type Galaxies*. pp 109–112

APPENDIX A: PRESSURE CONFINED CLOUDS

The truncated spherical equilibrium configurations studied by Shapiro et al. (1999) provide a convenient model for IGM clouds, because they contain two key physical ingredients: they are isothermal and confined by the pressure of an external medium. These configurations are described by solutions of a dimensionless Lane-Emden equation:

$$\frac{d}{d\zeta} \left[\zeta^2 \frac{d(\ln \bar{\rho})}{d\zeta} \right] = -\bar{\rho} \zeta^2 \quad (\text{A1})$$

Here $\zeta = r/r_0$ and $\bar{\rho} = \rho/\rho_0$ are defined as dimensionless distance and density, respectively. The characteristic scales are related by:

$$r_0 = \frac{\sigma}{(4\pi G \rho_0)^{1/2}} = \left(\frac{k_B T_{cl}}{4\pi G \rho_m \rho_0} \right)^{1/2} \quad (\text{A2})$$

where we have introduced the definition: $\sigma = (k_B T_{cl}/m_p)$, T_{cl} being the cloud's temperature. The TIS models studied by Shapiro et al. (1999) are exact solutions of the initial value problem for eq. A1 subject to two initial conditions at the origin:

$$\rho(\zeta = 0) = 1, \quad \frac{d\rho}{d\zeta} \Big|_{\zeta=0} = 0 \quad (\text{A3})$$

The first condition enforces the initial value for the density, while the second one selects those solutions which are not singular, i.e. it defines a *core*. These configurations still have infinitely extending density profiles decaying as r^{-2} for $r \ll r_0$, but in presence of an external pressure the profiles get truncated at a radius r_t (McCrea 1957). This

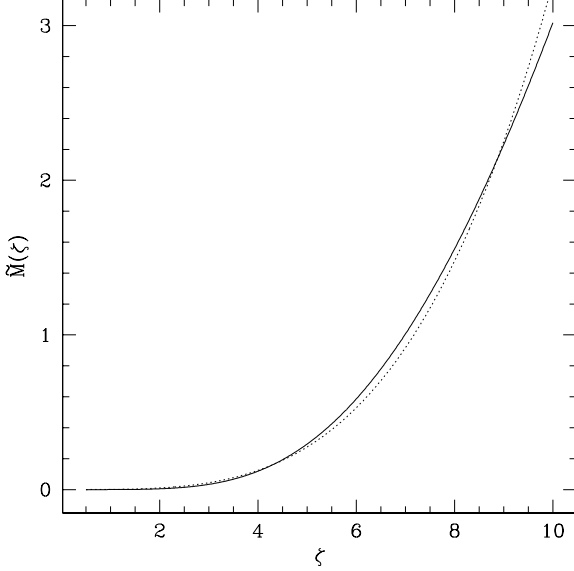


Figure A1. Power-law approximation to the TIS mass profile. The continuous curve is the function $\tilde{M}(\zeta)$, the dotted one the approximation eq. A6.

external confining pressure p_t is then an additional parameter, which will determine the dimensionless truncation distance ζ_t . Thus, these models are completely characterized by three parameters: p_t , the total cloud mass M_{cl} and radius r_t . From these we can deduce the characteristic density ρ_0 and scale r_0 , by assuming that clouds are described as TIS profiles. From eq. (35) of Shapiro et al. (1999) M_{cl} is expressed in terms of the averaged mass as:

$$M_t = \left(\frac{k_B T_{cl}}{G m_p} \right)^{3/2} \frac{\tilde{M}(\zeta_t)}{(4\pi \rho_0)^{1/2}} \quad (\text{A4})$$

where: $\zeta_t = r_t/r_0$ and we have defined:

$$\tilde{M}(\zeta) = \int_0^\zeta ds s^2 \tilde{\rho}(s) \quad (\text{A5})$$

In the interval $0 \leq \zeta \leq 9$ the following expression provides a good approximation to eq. A5 with the density $\tilde{\rho}(s)$ specified by the TIS solution:

$$\tilde{M}(\zeta) = \lambda \zeta_t^{1/\beta} \quad (\text{A6})$$

where the coefficient $\beta = 0.28 \pm 0.04$ has been introduced in eq. 3. This fit is accurate to 4%, as can also be seen from Fig. A1.

Inserting eq. A6 into eq. A4 and making use of the relationship between r_0 and ρ_0 (eq. A2) to eliminate ρ_0 , one obtains:

$$\left(\frac{\sigma^2}{G} \right)^{3/2} \frac{G^{1/2} r_0 \lambda}{\sigma} = c r_0^{1/\beta} \quad (\text{A7})$$

Finally, one arrives at an expression for r_0 :

$$r_0 = \left(\frac{k_B \lambda}{G m_p c} \right)^{\frac{\beta}{1-\beta}} T_{cl}^{\frac{\beta}{1-\beta}} \quad (\text{A8})$$

For the values of $\beta = 0.28 \pm 0.04$ and using for c and λ the values given above, one obtains:

$$r_0 = 0.248 T_{cl}^{0.32} pc \quad (\text{A9})$$

and:

$$\rho_0 = 2.48 \times 10^{18} M_\odot \text{Mpc}^{-3} \quad (\text{A10})$$

APPENDIX B: COOLING FUNCTION

We adopt the cooling function provided by Sutherland & Dopita (1993), for a metallicity $[\text{Fe}/\text{H}] = -1$, which should be valid in the temperature interval $10^4 < T < 10^8 \text{K}$. However, the shocked IGM plasma in our simulations often reaches temperatures higher than 10^8K , so we need to extend the cooling function to higher temperatures.

The cooling function for a fully ionized plasma in the trans-relativistic regime ($5 \times 10^7 < T < 5 \times 10^9 \text{K}$, see Wolfe & Melia 2006) has been computed by Svensson (1982), and includes contributions from different relevant processes like e^+e^- annihilations, and the related bremsstrahlung rates. Note that, in principle, cooling from e^+e^- annihilations is more than 2 orders of magnitudes higher than e^-p and e^-e^- bremsstrahlung cooling rates. However, in a relativistic thermal plasma the production of e^+e^- pairs starts to be significant at temperatures larger than the threshold for $\gamma\gamma \rightarrow e^+e^-$, i.e. for $T \geq 5.93 \times 10^9 \text{K}$. There exist few fits to Svensson's relativistic cooling function. Stepney & Guilbert (1983) provide a fit with 4 coefficients, each computed in tabulated form for different values of the temperature. For the more limited temperature interval relevant to our work, two approximate formulas are available from the literature. (Park & Ostriker 2001, eqs. A1-A4) provide the following fitting formulae:

$$\frac{\Lambda^{PO}}{n_e n_i} = \sigma_T c \alpha_f m_e c^2 n_i^2 \left[\left\{ \lambda_{br}(T_e) + 6.0 \times 10^{-22} \theta_e^{-1/2} \right\}^{-1} + \left(\frac{\theta_e}{4.82 \times 10^{-6}} \right)^{-12} \right]^{-1}, \quad (\text{B1})$$

where σ_T is the Thomson cross section, α_f the fine-structure constant, n_i the number density of ions, and $\theta_e \equiv kT_e/M_e c^2$. The bremsstrahlung cooling rate $\lambda_{br}(T_e)$ is given by:

$$\lambda_{br} = \left(\frac{n_e}{n_i} \right) \left(\sum_i Z_i^2 \right) F_{ei}(\theta_e) + \left(\frac{n_e}{n_i} \right)^2 F_{ee}(\theta_e) \quad (\text{B2})$$

where

$$\begin{aligned} F_{ei} &= 4 \left(\frac{2}{\pi^3} \right)^{1/2} \theta_e^{1/2} (1 + 1.781 \theta_e^{1.34}) & \theta_e < 1 \\ &= \frac{9}{2\pi} \theta_e [\ln(1.123 \theta_e + 0.48) + 1.5] & \theta_e > 1 \\ F_{ee} &= \frac{5}{6\pi^{3/2}} (44 - 3\pi^2) \theta_e^{3/2} (1 + 1.1 \theta_e + \theta_e^2 - 1.25 \theta_e^{5/2}) & \theta_e < 1 \\ &= \frac{9}{\pi} \theta_e [\ln(1.123 \theta_e) + 1.2746] & \theta_e > 1. \end{aligned}$$

This fit is claimed to be accurate to 2% over the full transrelativistic domain.

A relatively simpler fit has been provided by Krause & Alexander (2007):

$$\frac{\Lambda^{KA}}{n_e n_i} = 2.05 \times 10^{-27} \sqrt{T} (1 + 4.4 \times 10^{-10} T) \quad (\text{B3})$$

(Note that we have adopted units of $\text{erg} \cdot \text{cm}^3 \cdot \text{sec}^{-1}$ in both eqs. 1 and 2). We show these fits in fig. B1. This latter figure

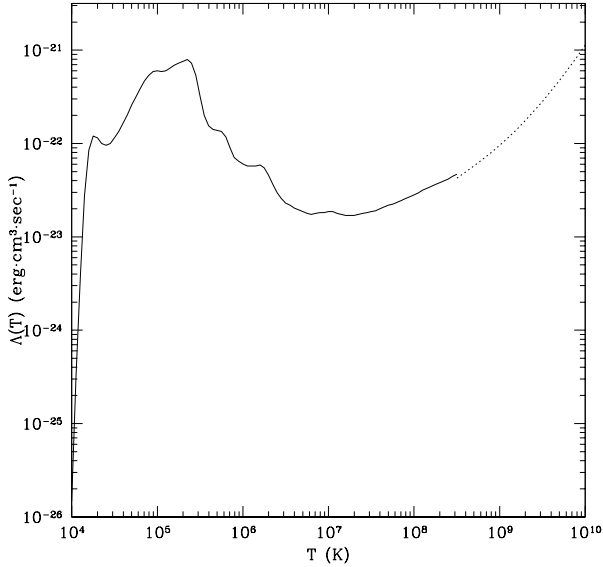


Figure B1. The adopted cooling function. The continuous line denotes the Sutherland & Dopita 1993 cooling function, while the dotted line is the approximation we have adopted for $T \geq 10^{8.5}$ K, from Krause & Alexander 2005.

should be compared with Fig. 9 of Svensson (1982). Svensson label the different curves according to the *thickness parameter* $\tau_{n_i} = n_i r_e^2 R = 2.436 \times 10^{-7} n_i [\text{cm}^{-3}] R [\text{pc}]$, where: r_e is the electron radius and R is a typical size of the jet. It is clear that, for all the cases we consider, one has $\tau_{n_i} \ll 1$, so we can neglect the contribution from thermally-produced pairs to the cooling function, which is also dominated by bremsstrahlung in this temperature range.

Note however that no equilibrium relativistic plasma configuration is possible for $\theta_e > 1$ (the curve labeled as “O” in Fig. 9 of Svensson (1982), corresponding to $\theta_{max} = 25$, or: $T_{max} = 1.48 \times 10^{11} K$). At this critical maximum temperature essentially all the plasma is converted to pairs, which then can leave the volume and annihilate outside. For $T \geq T_{max}$ we then assume $\lambda \rightarrow \infty, n_e \rightarrow 0$. The plasma is left with ions, at a significantly lower temperature.